J Mol Model (2013) 19:5469–5477
DOI 10.1007/s00894-013-2004-8

ORIGINAL PAPER

A refined parameterization of the analytical Cd–Zn–Te bond-order potential

Donald K. Ward · Xiaowang Zhou · Bryan M. Wong · F. Patrick Doty

Received: 24 July 2013 / Accepted: 8 September 2013 / Published online: 13 November 2013

Abstract This paper reports an updated parameterization for a CdTe bond order potential. The original potential is a rigorously parameterized analytical bond order potential for ternary the Cd–Zn–Te systems. This potential effectively captures property trends of multiple Cd, Zn, Te, CdZn, CdTe, ZnTe, and $Cd_{1-x}Zn_xTe$ phases including clusters, lattices, defects, and surfaces. It also enables crystalline growth simulations of stoichiometric compounds/alloys from non-stoichiometric vapors. However, the potential over predicts the zinc-blende CdTe lattice constant compared to experimental data. Here, we report a refined analytical Cd–Zn–Te bond order potential parameterization that predicts a better CdTe lattice constant. Characteristics of the second potential are given based on comparisons with both literature potentials and the quantum mechanical calculations.

Keywords Cadmium zinc telluride · Molecular dynamics · Bond-order potential

D. K. Ward (✉) · F. P. Doty
Radiation and Nuclear Detection Materials and Analysis Department, Sandia National Laboratories, Livermore CA 94550, USA
e-mail: donward@sandia.gov

X. Zhou
Mechanics of Materials Department, Sandia National Laboratories, Livermore, CA 94550, USA

B. M. Wong
Department of Chemistry and Department of Materials Science and Engineering, Drexel University, Philadelphia PA 19104, USA

Introduction

II–VI semiconductor compounds such as CdTe and $Cd_{1-x}Zn_xTe$ are used widely for radiation detection [1] and solar cell applications [2]. The performance of these materials is limited by various atomic/micro scale defects [3–6]. In order to enable high-fidelity atomistic simulations of defects in these materials, we recently developed an analytical Cd–Zn–Te bond-order potential (BOP) [7–12] and incorporated it in advanced molecular dynamics codes LAMMPS [13]. This analytical BOP was derived directly from quantum mechanical theories by Pettifor and collaborators [14–16] considering both σ and π bonding effects. Therefore, it is fundamentally far more transferable than other empirical interatomic potentials [17–20]. In particular, our first parameterization of the potential indicates that the BOP not only captures well the property trends of a variety of Cd, Zn, Te, CdZn, CdTe, ZnTe, and $Cd_{1-x}Zn_xTe$ phases including clusters, lattices, defects, and surfaces, but also enables the correct crystalline growth simulations of various ground state phases under a variety of chemical vapor deposition conditions [7–12, 21]. One deficiency of our previous parameterization (termed as BOPa), however, is that it over predicts the zinc-blende (zb) CdTe lattice constant as compared to the experimental data. Here, we provide a refined parameterization of the analytical Cd–Zn–Te BOP (termed as BOPb) that removes this problem while maintaining the transferability of the original parameterization. Modifying a BOP parameterization is not a trivial task and requires the same rigorous testing as the first parameterization. Details of the formalisms and parameterization procedures of the potential have been described in great detail previously [7, 8] and hence we have included a brief review of the potential in "BOP formulation and parameterization" section. During the parameterizing, DFT values are used as reference and target values for the fitting process. The methods used for the DFT calculations are described in "DFT methods" section and [7].

Materials and methods

BOP formulation and parameterization

For BOP formulation and parameterization, see Appendix. For more detailed discussion and descriptions of all equations, please see [7].

An effective approach to ensure a highly transferable, growth-simulation-enabling interatomic potential for semiconductors is to directly fit (or at least monitor) the atomic volumes, cohesive energies, and elastic properties of a correct set of target structures. The target structures included are listed in [7]. While all these phases are not used in a particular parameterization, monitoring the energies of many structures helps select the important ones and their weighting factors for fitting to ensure the lowest energies for the equilibrium phases.

Appropriate target structures and fitting methods alone are not sufficient to create a physically sound BOP. Many parameters critically require valid bounds. It is not trivial to determine the bounds of all the parameters. The bounds of the parameters that we used do not necessarily represent the optimum choices, but were obtained from a combination of physical intuition and extensive trial-and-error experimentations. One physical requirement described in [7] determines m/n to be near 2.0. In addition, the pair function parameters are constrained so that Eqs. (5)–(7) decay to small values near the cutoff distances even without multiplying them by the cutoff function. Finally, the parameters of the angular function are constrained so that Eq. (10) is monotonic between θ=0° and θ=180°.

The fitting procedure follows a similar method to that of Albe et al. [24] used to parameterize Tersoff potentials. Symbolic computations were performed using Mathematica [25] to derive complicated expressions for the cohesive energies, pressure, and elastic constants of various structures. Four Mathematica built-in numerical optimization routines, namely a conjugate gradient method [26]; the downhill simplex method of Nelder and Mead [27]; a genetic algorithm [28]; and biased random walk (simulated annealing) [29], were all used to determine the parameters that minimize the mean-square difference between the target and predicted properties (bond length, bond energy, and bulk modulus). Further discussion and description of these processes are included in [7].

DFT methods

Our DFT results are obtained using the same techniques as our previous work [7, 8]. The simulations were based on spin-polarized, generalized gradient approximation (GGA) methods using projector-augmented-wave (PAW) pseudopotentials with a dispersion-corrected Perdew-Burke-Ernzerhof (PBE-D2) functional [30]. Within the DFT-D2 approach [31, 32], an atomic pair-wise dispersion correction is added to the Kohn-Sham part of the total energy ($E_{\text{KS-DFT}}$) as

$$E_{\text{DFT}-\text{D}} = E_{\text{KS}-\text{DFT}} + E_{\text{disp}}, \tag{1}$$

where E_{disp} is given by

$$E_{\text{disp}} = -s_6 \sum_{i=1}^{N_{\text{at}}-1} \sum_{j=i+1}^{N_{\text{at}}} \sum_{\mathbf{g}} f_{\text{damp}}\left(R_{ij,\mathbf{g}}\right) \frac{C_6^{ij}}{R_{ij,\mathbf{g}}^6}. \tag{2}$$

Here, the summation is over all atom pairs i and j, and over all $\mathbf{g}$ lattice vectors with the exclusion of the $i = j$ contribution when $\mathbf{g}=0$ (this restriction prevents atomic self-interaction in the reference cell). The parameter C_6^{ij} is the dispersion coefficient for atom pairs i and j, calculated as the geometric mean of the atomic dispersion coefficients: $C_6^{ij} = \sqrt{C_6^i C_6^j}$.

The s_6 parameter is a global scaling factor, which is specific to the adopted DFT method (s_6=0.75 for PBE), and $R_{\text{ij},\mathbf{g}}$ is the interatomic distance between atom i in the reference cell and j in the neighboring cell at distance $|\mathbf{g}|$. A cutoff distance of 30.0 Å was used to truncate the lattice summation. In order to avoid near-singularities for small interatomic distances, the damping function has the form

$$f_{\text{damp}}\left(R_{ij,\mathbf{g}}\right) = \frac{1}{1 + \exp\left[-d\left(R_{ij,\mathbf{g}}/R_{\text{vdW}} - 1\right)\right]}, \tag{3}$$

where R_{vdW} is the sum of atomic van der Waals radii ($R_{\text{vdW}} = R_{\text{vdW}}^{\text{i}} + R_{\text{vdW}}^{\text{j}}$), and d controls the steepness of the damping function.

For all the small-cluster and bulk-lattice calculations, we used a very high cutoff energy of 500 eV for the plane-wave basis set, and the Brillouin zone was sampled using a dense 10×10×10 Gamma-centered Monkhorst-Pack grid. In addition to spin-polarization and dispersion effects, we also included a relativistic spin-orbit coupling treatment for all the valence electrons in both the small-clusters and bulk-lattice calculations. Unconstrained geometry optimizations of both the ions and the unit cell were carried out. To prevent spurious interactions between adjacent clusters for the small-cluster calculations, the vacuum along all 3 axes was set to 25 Å during the geometry optimization.

Table 1 Global and point-dependent bond-order potential (BOP) parameters

Symbol	ζ_1	ζ_2	ζ_3	ζ_4	$p_{\pi,\text{Cd}}$	$p_{\pi,\text{Te}}$	$p_{\pi,\text{Zn}}$
Value	0.00001	0.00001	0.00100	0.00001	0.420000	0.460686	0.420000

Table 2 Pair-dependent CdTe BOPb parameters (BOPa parameters in parenthesis when different)

Symbol	r_0	r_c	r_1	r_{cut}	n_c
Value	2.96765 (3.1276)	2.96765 (3.1276)	3.80853 (4.0138)	4.64941 (4.9000)	2.811251
Symbol	m	n	ϕ_0	$\beta_{\sigma,0}$	$\beta_{\pi,0}$
Value	2.388647 (2.5878331)	1.188381 (1.287478)	0.654330 (0.631440)	0.836402 (0.825290)	0.030748 (0.031743)
Symbol	c_σ	f_σ	k_σ	c_π	a_π
Value	1.196365 (1.286955)	0.500000	0	1	1

Since the point-defect and surface calculations require the use of larger supercells and significantly more atoms (>200 atoms), a smaller 300 eV cutoff energy was used for both calculations. For this same reason, we did not include spin-orbit effects in these large supercell systems, although we still carried out these calculations with unconstrained spin-polarized conditions. In the point-defect calculations, a large 3×3×3 supercell was used and, therefore, a smaller 2×2×2 Gamma-centered Monkhorst-Pack grid was utilized. For the surface calculations, a slab geometry was chosen, which consisted of seven layers of CdTe and 35 Å of vacuum between adjacent slabs. In these calculations, a 4×4×1 Gamma-centered Monkhorst-Pack grid was utilized. Unconstrained geometry optimizations of both the ions and the unit cell were carried out.

Results and discussion

A complete list of the parameters for BOPb is summarized in Tables 1, 2 and 3 for global/point, pair, and three-body parameters, respectively, with the original parameters from BOPa in parenthesis when they differ.

Compared with BOPa, BOPb modifies only the Cd–Te pair parameters and Cd–Zn–Te three-body parameters, resulting in changes only to the properties of binary Cd–Te and ternary Cd–Zn–Te phases. As a result, only these phases are considered. To examine numerically the transferability of sizes and energies to different CdTe environments, bond lengths/lattice parameters and cohesive energies of different Cd–Te clusters (bond lengths) and lattices (lattice parameters) obtained from BOPb are compared in Table 4 with those [7] obtained from density function theory (DFT) calculations, BOPa, Stillinger-Weber (SW) [17], Tersoff-Rockett (TR) [20], and experiments [22]. Table 4 indicates that, for the equilibrium CdTe-zb structure, BOPb indeed improves over BOPa on reproducing more closely the experimental lattice constant whereas the cohesive energy remains approximately unchanged. To clearly see the lattice parameter and energy trends of other metastable phases, Table 4 is reproduced in Figure 1a,b for atomic volume (related to lattice parameter) and cohesive energy, respectively, where the volumes and energies are normalized against the respective values of the lowest volume or energy structure as determined from DFT (see "DFT methods"

Table 3 Three-body-dependent BOPb parameters (with BOPa parameters in parenthesis when different)

Symbol	Cd-centered triples *j*-Cd-*k*					
	CdCdCd	CdCdTe	CdCdZn	TeCdTe	TeCdZn	ZnCdZn
g_0	1	1	1	1	1	1
b_σ	0.762039	0.208810 (1.000000)	0.433692	0.200000	0.824321 (0.882784)	0.455028
u_σ	−0.400000	−0.168759 (0.099711)	0.100000	−0.400000 (−0.383360)	0.015663 (0.100000)	−0.085972
Symbol	Te-centered triples *j*-Te-*k*					
	CdTeCd	CdTeTe	CdTeZn	TeTeTe	TeTeZn	ZnTeZn
g_0	1	1	1	1	1	1
b_σ	0.259985 (0.200000)	0.807985 (0.999854)	0.422411 (0.364627)	0.669623	0.734966	0.200000
u_σ	−0.400000	0.022436 -(0.003929)	−0.333333	−0.141521	0.100000	−0.400000
Symbol	Zn-centered triples *j*-Zn-*k*					
	CdZnCd	CdZnTe	CdZnZn	TeZnTe	TeZnZn	ZnZnZn
g_0	1	1	1	1	1	1
b_σ	0.200000	0.831080 (0.939572)	0.758047	0.200000	1.000000	1.000000
u_σ	−0.223201	0.100000 (−0.400000)	0.100000	−0.400000	−0.001972	−0.400000

Table 4 Energies E (eV) and bond distances (clusters)/lattice parameters (lattices) *a, c* (Å) for various CdTe clusters and lattices obtained from different models. Cluster abbreviations: *di* dimer, *tri* trimer, *rhom* rhombus; lattice abbreviations: *B1* NaCl, *B2* CsCl, *wz* wurtzite, *zb* zinc-blende

Structure	DFT[a] (exp)*		BOPa[a]		BOPb		SW[b]		TR[c]	
	a,c(Å)	E_c	a,c(Å)	E_c	a,c(Å)	E_c	a,c(Å)	E_c	a,c(Å)	E_c
di	2.61	−0.519	2.92	−0.596	2.77	−0.588	2.82	−0.515	2.77	−0.573
tri (Cd_2Te)	2.81	−0.561	2.85	−0.641	2.85	−0.639	2.82	−0.687	2.77	−0.764
	3.47		3.09		2.94		4.60		4.96	
tri ($CdTe_2$)	4.07	−1.269	2.80	−1.131	2.80	−1.162	3.12	−0.695	2.91	−0.775
	2.59		3.20		3.02		3.10		3.01	
rhom	2.77	−1.306	3.11	−1.057	2.94	−1.106	2.88	−0.952	2.88	−0.993
B1	6.04	−2.287	6.19	−2.140	6.12	−2.056	6.35	−1.796	5.85	−2.177
B2	3.81	−2.006	3.83	−1.656	3.95	−1.663	3.94	−1.719	3.63	−2.339
wz	4.52	−2.279	4.84	−2.173	4.59	−2.149	3.98	−2.060	3.97	−2.060
	7.32		7.88		7.49		7.51		7.49	
zb	6.52 (6.48[d])*	−2.331 (−2.178[e])*	6.83	−2.173	6.48	−2.149	6.51	−2.060	6.49	−2.060

* Experimental values for the equilibrium zinc-blende CdZn

[a] DFT and BOPa data [7]

[b] Stillinger-Weber (SW) data [17]

[c] Tersoff-Rockett (TR) data [20]

[d] Experimental data [33]

[e] Experimental data [22]

section). Clearly, BOPb retains approximately the volume and energy trends of BOPa, which improves over other potentials, especially considering that BOPs are also transferable to elemental Cd, and Te environments where the SW and TR potentials give incorrect lowest energy phases.

The compositions of ternary systems are bounded by Cd, Zn, Te elements and CdTe, CdZn, and TeZn binary phases. With the correct trends of atomic volumes and energies of various elemental and binary environments verified, the most important properties to capture for the ternary systems are the lowest energy phase and the energy trends at different compositions compounds. The lowest energy phase can be tested most effectively using vapor deposition simulations as will be described below. Here we examine the energy trends using five compounds with increasing Zn content: CdTe (zb), Cd_3ZnTe_4 (sulvanite), $CdZnTe_2$ (tetragonal *p4m2*), $CdZn_3Te_4$ (sulvanite), and ZnTe (zb). The energy trends calculated from various models are shown in Figure 2. It can be seen that BOPb and BOPa have similar magnitudes of energy, which are higher than the DFT values. This is because the BOPs are fitted to experimental energies of CdTe and ZnTe zinc-blende

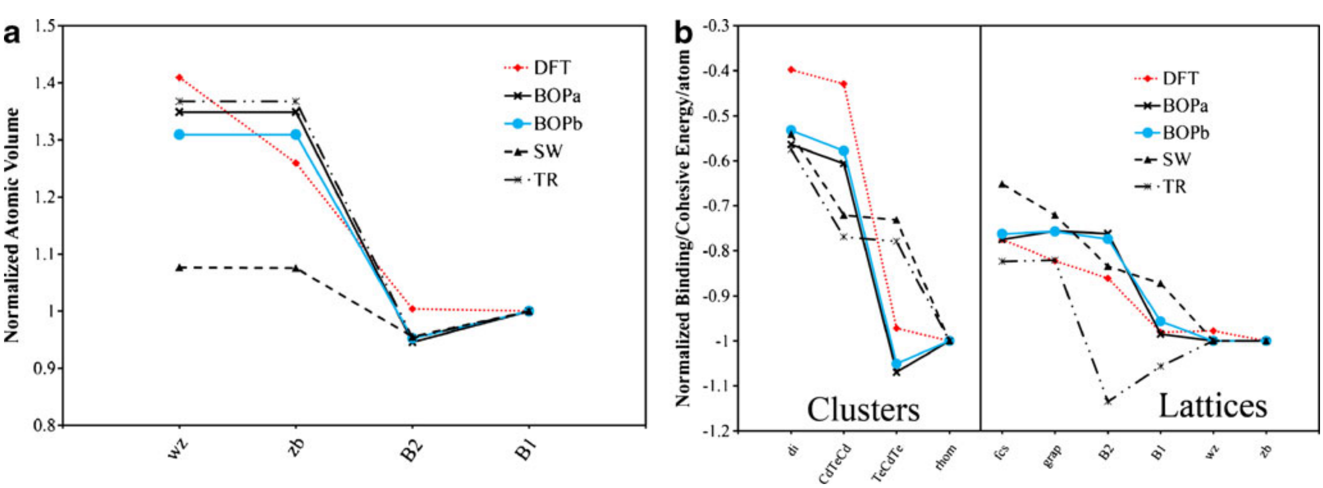

Fig. 1 (Color online) Normalized **a** atomic volumes and **b** cluster and lattice binding/cohesive energies for a variety of CdTe structures

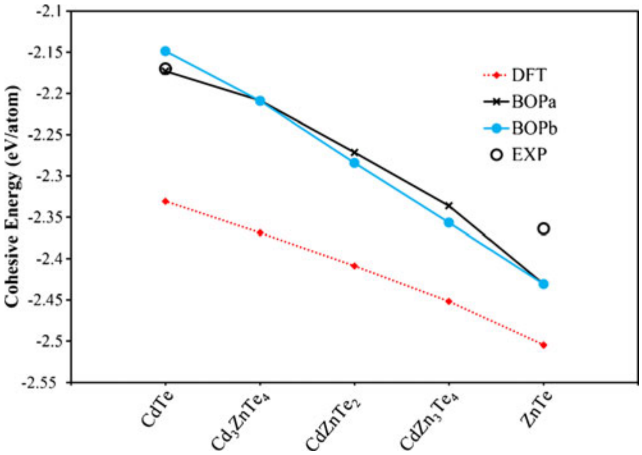

Fig. 2 (Color online) Cohesive energies for various CdZnTe compounds

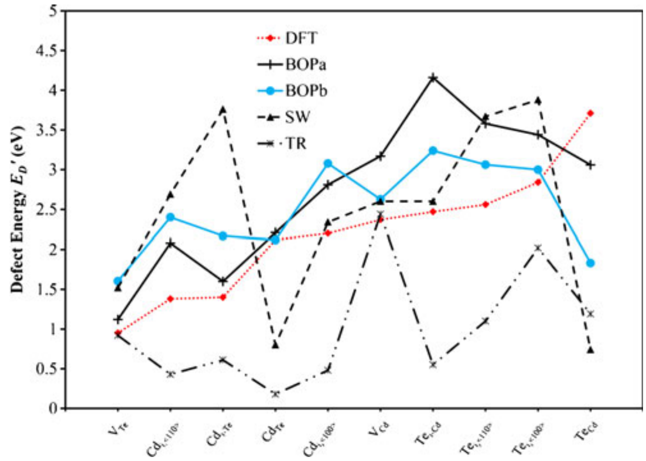

Fig. 3 (Color online) Various defect energies of the CdTe-zb phase

structures that do not necessarily match exactly the DFT values. On the other hand, BOPb does predict a less curvature of the energy vs structure curve, which seems to match better with the DFT results.

Elastic constants and melting temperature of the CdTe-zb structure were also calculated following the previous approach [7]. The results obtained from different models are shown in Table 5. While c_{11} and c_{12} are slightly lower than the experimental values, the general agreement between BOPb and experiments is maintained. In addition, BOPb predicts a melting temperature of 1350–1430 K, closer to the experimental value than BOPa.

For zinc-blende CdTe, the previous method [7] was also used to calculate the energies of various defects including Cd vacancy (V_{Cd}), Te vacancy (V_{Te}), Cd at Te antisite (Cd_{Te}), Te at Cd antisite (Te_{Cd}), Cd interstitial surrounded by the Te tetrahedron shell (Cd_i), Te interstitial surrounded by the Cd tetrahedron shell (Te_i), and <110> and <100> dumbbell interstitials. The defect energies obtained from different models are compared in Fig. 3. It can be seen that BOPb retains the energy sequence of BOPa very well, except for Te_{Cd}, which is substantially reduced.

CdTe surface reconstructions are also examined. Figure 4 shows the energies (Γ) of various surface reconstructions as a function of the chemical potential difference ($\Delta\mu$) as calculated from BOPb (see [7] for details). It can be seen from Figure 4 that BOPb predicts surface dimers to be stable for the Cd terminated surfaces with a coverage (ξ) of 1.0 [i.e., Cd-c(1x2) surface]. BOPa, on the other hand, predicts that the surface dimers are unstable [7]. Experimentally, dimer separation has been seen, yet the DFT simulations predict dimerization. In addition, BOPb predicts Te-c(2×2) and Cd-(1×2) (coverage 1.0) as the low energy reconstructions for Te-rich ($\Delta\mu<0$) and Cd-rich ($\Delta\mu>0$) conditions, respectively, whereas BOPa predicts Te-(2×1) and Cd-(1×1) (coverage 1.0) as the low energy reconstructions for Te-rich and Cd-rich conditions, respectively. Both of these differ from the DFT results, which predict low energy reconstructions of Cd-(2×1) and Cd-c(2×2) both with coverage of 0.5.

Table 5 Elastic constants c_{ij} $(i, j=1, 2, 4)$ (GPa) and melting temperature T_m (K) of the zinc-blende CdTe

Property	exp	DFT[b]	BOPa[c]	BOPb	SW[d]	TR[e]
c_{11} (GPa)	53.3[f]	53.2	53.2	51.6	44.3	50.7
c_{12} (GPa)	36.5[f]	36.0	36.0	29.2	19.6	37.5
c_{44} (GPa)	20.4[f]	–	16.4	21.0	18.0	15.2
$c_{44}{}^{a}$ (GPa)	–	31.8	40.6	42.4	30.7	46.8
T_m (K)	1,365[g]	–	1,550–1,600	1,350–1,430	1,360–1,390	700–800

[a] Unrelaxed

[b] DFT data [34]

[c] BOPa data [7]

[d] Stillinger-Weber (SW) data [17]

[e] Tersoff-Rockett (TR) data [20]

[f] Experimental data at 300 K [35]

[g] Experimental data [36]

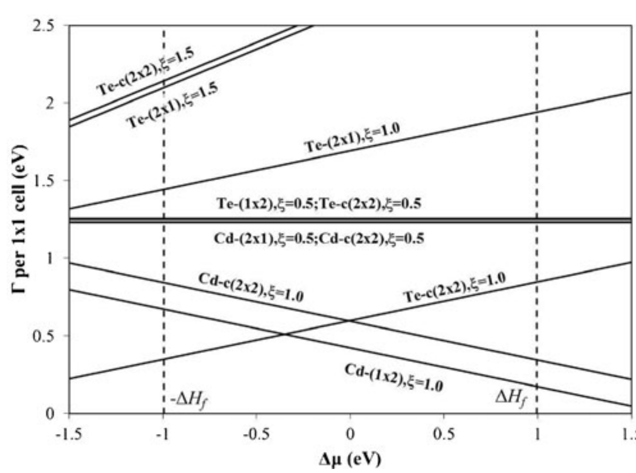

Fig. 4 (010) CdTe surface energy phase diagrams predicted by BOPb

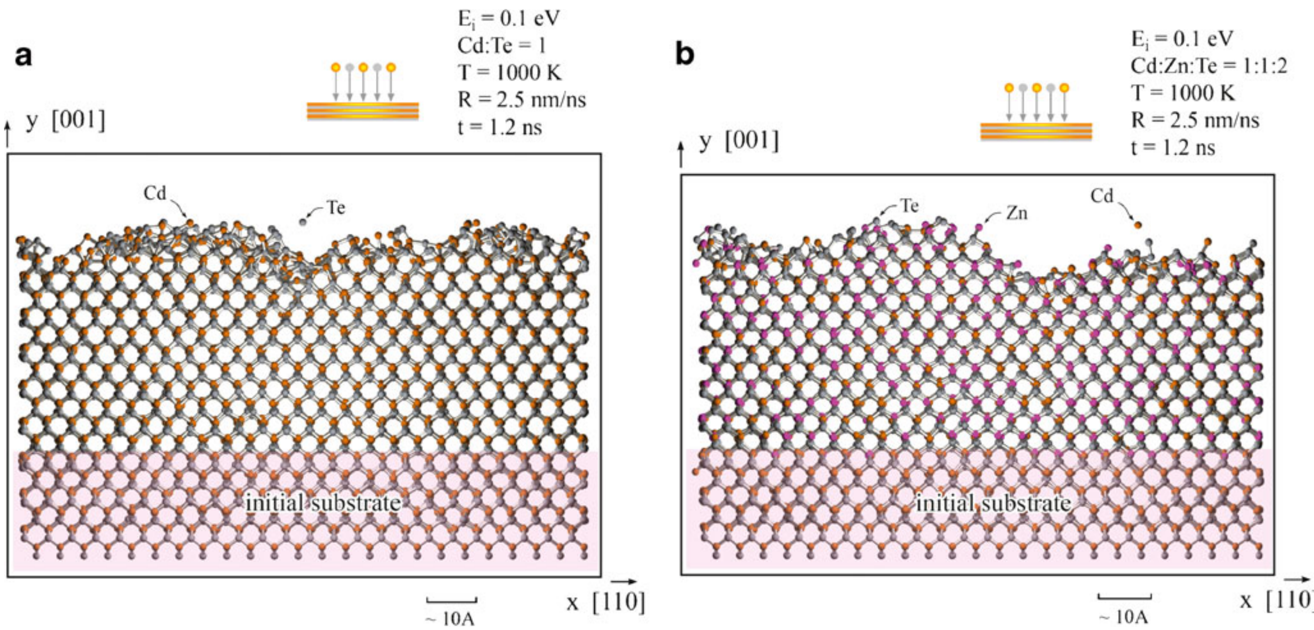

Fig. 5a.b (Color online) Growth structure predicted by BOPb. **a** CdTe, **b** zb-$Cd_{0.5}Zn_{0.5}Te$ deposited on an initial (010) zb-CdTe substrate shaded in *pink*

Vapor deposition simulations sample a variety of configurations by injecting adatoms at random locations and random compositions on the surface of a ground state phase. The structures sampled through vapor deposition are not predetermined and are therefore the most important tests to validate the transferability of a potential. If a potential correctly captures the lowest energy for the ground state phase, a crystalline, stoichiometric growth would be predicted even for non-stoichiometric vapor fluxes. Potentials that capture the incorrect lowest energy grounds state phase would likely result in an amorphous growth [7]. As inherited from BOPa, BOPb can predict the crystalline growth of hexagonal close packed (hcp) Cd, hcp Zn, A8 Te, and zb ZnTe [7, 8]. Figure 5a,b shows vapor depositions simulations of CdTe and $Cd_{0.5}Zn_{0.5}Te$, respectively, on a (010) zb CdTe substrate, using BOPb and the same simulation technique as BOPa [7]. These simulations verify that BOPb can predict the crystalline growth of CdTe and $Cd_{1-x}Zn_xTe$ on alloyed compounds.

In summary, we have parameterized a second analytical bond order potential BOPb for the Cd-Zn-Te ternary systems. This new potential more accurately captures the lattice constant for the zinc-blende CdTe phase while maintaining the general property trends of the old potential. In fact, the only noticeable difference is that BOPb predicts a substantially lower Te_{Cd} defect energy. Like the old potential, BOPb can predict crystalline growth of CdTe and $Cd_{1-x}Zn_xTe$. This not only verifies the transferability of the potential, but also allows the defects to be studied from growth simulations without any assumptions regarding defect configurations and formation mechanisms. Many previous potentials lack such a crystalline growth simulation capability [21].

Acknowledgments This work is supported by the National Nuclear Security Administration (NNSA)/Department of Energy (DOE) Office of Nonproliferation Research and Development, Proliferation Detection Program, Advanced Materials Portfolio. Sandia National Laboratories is a multi-program laboratory managed and operated by Sandia Corporation, a wholly owned subsidiary of Lockheed Martin Corporation, for the US DOE's National Nuclear Security

Appendix

For the BOP formulation the total energy of a system is expressed as

$$E = \frac{1}{2}\sum_{i=1}^{N}\sum_{j=i_1}^{i_N}\phi_{ij}(r_{ij}) - \sum_{i=1}^{N}\sum_{j=i_1}^{i_N}\beta_{\sigma,ij}(r_{ij})\cdot\Theta_{\sigma,ij} - \sum_{i=1}^{N}\sum_{j=i_1}^{i_N}\beta_{\pi,ij}(r_{ij})\cdot\Theta_{\pi,ij} \tag{4}$$

where $\phi_{ij}(r_{ij})$ is a short-range two-body potential, $\beta_{\sigma,ij}(r_{ij})$ and $\beta_{\pi,ij}(r_{ij})$ are, respectively, σ and π bond integrals, $\Theta_{\sigma,ij}$ and $\Theta_{\pi,ij}$ are σ and π bond-orders. $\phi_{ij}(r_{ij})$, $\beta_{\sigma,ij}(r_{ij})$, and $\beta_{\pi,ij}(r_{ij})$ are expressed in a general form as

$$\phi_{ij}(r_{ij}) = \phi_{0,ij} \cdot f_{ij}(r_{ij})^{m_{ij}} \cdot f_{c,ij}(r_{ij}) \tag{5}$$

$$\beta_{\sigma,ij}(r_{ij}) = \beta_{\sigma,0,ij} \cdot f_{ij}(r_{ij})^{n_{ij}} \cdot f_{c,ij}(r_{ij}) \tag{6}$$

$$\beta_{\pi,ij}(r_{ij}) = \beta_{\pi,0,ij} \cdot f_{ij}(r_{ij})^{n_{ij}} \cdot f_{c,ij}(r_{ij}) \tag{7}$$

where $f_{ij}(r_{ij})$ is a Goodwin-Skinner-Pettifor (GSP) radial function [23], and $f_{c,ij}(r_{ij})$ is a cutoff function (see [7] for formulation). Furthermore, $\Theta_{\sigma,ij}$ is given by:

$$\Theta_{\sigma,ij} = \Theta_{s,ij}\left(\Theta_{\sigma,ij}^{(1/2)}, f_{\sigma,ij}\right) \cdot \left[1 - \left(f_{\sigma,ij} - \frac{1}{2}\right) \cdot k_{\sigma,ij} \cdot \frac{\beta_{\sigma,ij}^2(r_{ij}) \cdot R_{3\sigma,ij}}{\beta_{\sigma,ij}^2(r_{ij}) + \frac{\beta_{\sigma,ij}^2(r_{ij}) \cdot \Phi_{2\sigma}^i + \beta_{\sigma,ij}^2(r_{ij}) \cdot \Phi_{2\sigma}^j}{2} + \zeta_2}\right] \tag{8}$$

Where, $\Phi_{2\sigma}^{i}$ and $\Phi_{2\sigma}^{j}$ are local variables arising from electron hop paths. In addition, $\Phi_{2\sigma}^{i}$ and $\Phi_{2\sigma}^{j}$ have the same formulation but are merely evaluated for atoms i and j, respectively. Since only the product of $\beta_{\sigma,ij}^2(r_{ij}) \cdot \Phi_{2\sigma}^i$ is required for Eq. (8), the formulations are given as:

$$\beta_{\sigma,ij}^2(r_{ij}) \cdot \Phi_{2\sigma}^i = \sum_{\substack{k=i_1 \\ k \neq j}}^{i_N} g_{\sigma,jik}^2(\theta_{jik}) \cdot \beta_{\sigma,ik}^2(r_{ik}) \tag{9}$$

where θ_{jik} is the bond angle at atom i spanning atoms j and k, and the function $g_{\sigma,jik}(\theta_{jik})$ introduces angular-dependent contributions to the bonding resulting from the overlap of the hybridized atomic orbital. The three-body angular function is written as

$$g_{\sigma,jik}(\theta_{jik}) = \frac{\left(b_{\sigma,jik} - g_{0,jik}\right) \cdot u_{\sigma,jik}^2 - \left(g_{0,jik} + b_{\sigma,jik}\right) \cdot u_{\sigma,jik}}{2 \cdot \left(1 - u_{\sigma,jik}^2\right)} + \frac{g_{0,jik} + b_{\sigma,jik}}{2} \cdot \cos\theta_{jik} + \frac{g_{0,jik} - b_{\sigma,jik} + \left(g_{0,jik} + b_{\sigma,jik}\right) \cdot u_{\sigma,jik}}{2 \cdot \left(1 - u_{\sigma,jik}^2\right)} \cdot \cos^2\theta_{jik} \tag{10}$$

where $g_{\sigma,jik}$, $b_{\sigma,jik}$, and $u_{\sigma,jik}$ are three-body-dependent parameters. The half full valance bond order is given by:

$$\Theta_{\sigma,ij}^{(1/2)} = \frac{\beta_{\sigma,ij}(r_{ij})}{\sqrt{\beta_{\sigma,ij}^2(r_{ij}) + c_{\sigma,ij} \cdot \left[\beta_{\sigma,ij}^2(r_{ij}) \cdot \Phi_{2\sigma}^i + \beta_{\sigma,ij}^2(r_{ij}) \cdot \Phi_{2\sigma}^j\right] + \zeta_1}} \tag{11}$$

Equation (8) also requires knowing $\beta_{\sigma,ij}{}^2(r_{ij}) \cdot R_{3\sigma,ij}$ given by

$$\beta_{\sigma,ij}^2(r_{ij}) \cdot R_{3\sigma,ij} = \sum_{\substack{k=i_1 \\ k,j=n}}^{i_N} g_\sigma(\theta_{jik}) \cdot g_\sigma(\theta_{ijk}) \cdot g_\sigma(\theta_{ikj}) \cdot \beta_{\sigma,ik}(r_{ik}) \cdot \beta_{\sigma,jk}(r_{jk}) \tag{12}$$

The symmetric band-filling function is expressed as the continuous function

$$\Theta_{s,ij}\left(\Theta_{\sigma,ij}^{(1/2)}, f_{\sigma,ij}\right) = \frac{\Theta_0 + \Theta_1 + S \cdot \Theta_{\sigma,ij}^{(1/2)} - \sqrt{\left(\Theta_0 + \Theta_1 + S \cdot \Theta_{\sigma,ij}^{(1/2)}\right)^2 - 4\left(-\varepsilon\sqrt{1+S^2} + \Theta_0 \cdot \Theta_1 + S \cdot \Theta_1 \cdot \Theta_{\sigma,ij}^{(1/2)}\right)}}{2} \tag{13}$$

where

$$\begin{cases} \varepsilon = 10^{-10} \\ \Theta_0 = 15.737980 \cdot \left(\frac{1}{2} - \left|f_{\sigma,ij} - \frac{1}{2}\right|\right)^{1.137622} \cdot \left|f_{\sigma,ij} - \frac{1}{2}\right|^{2.087779} \\ S = 1.033201 \cdot \left\{1 - \exp\left[-22.180680 \cdot \left(\frac{1}{2} - \left|f_{\sigma,ij} - \frac{1}{2}\right|\right)^{2.689731}\right]\right\} \\ \Theta_1 = 2 \cdot \left(\frac{1}{2} - \left|f_{\sigma,ij} - \frac{1}{2}\right|\right) \end{cases} \tag{14}$$

The π bond-order $\Theta_{\pi,ij}$ used in Eq. (4) is expressed as

$$\Theta_{\pi,ij} = \frac{a_{\pi,ij} \cdot \beta_{\pi,ij}(r_{ij})}{\sqrt{\beta^2_{\pi,ij}(r_{ij}) + c_{\pi,ij} \cdot \left(\frac{\beta^2_{\pi,ij}(r_{ij}) \cdot \Phi^i_{2\pi} + \beta^2_{\pi,ij}(r_{ij}) \cdot \Phi^j_{2\pi}}{2} + \sqrt{\beta^4_{\pi,ij}(r_{ij}) \cdot \Phi_{4\pi} + \zeta_3}\right) + \zeta_4}} + \frac{a_{\pi,ij} \cdot \beta_{\pi,ij}(r_{ij})}{\sqrt{\beta^2_{\pi,ij}(r_{ij}) + c_{\pi,ij} \cdot \left(\frac{\beta^2_{\pi,ij}(r_{ij}) \cdot \Phi^i_{2\pi} + \beta^2_{\pi,ij}(r_{ij}) \cdot \Phi^j_{2\pi}}{2} - \sqrt{\beta^4_{\pi,ij}(r_{ij}) \cdot \Phi_{4\pi} + \zeta_3} + \sqrt{\zeta_3}\right) + \zeta_4}} \tag{15}$$

where $a_{\pi,ij}$ and $c_{\pi,ij}$ are pair parameters, ζ_3 and ζ_4 are constants, and $\Phi^i_{2\pi}$,$\Phi^j_{2\pi}$, $\Phi_{4\pi}$ are local variables.

The $\beta^2_{\pi,ij}(r_{ij})\cdot\Phi^i_{2\pi,ij}$ and $\beta^4_{\pi,ij}(r_{ij})\cdot\Phi_{4\pi,ij}$ terms used in Eq. (15) can be written as

$$\beta^2_{\pi,ij}(r_{ij}) \cdot \Phi^i_{2\pi,ij} = \sum_{\substack{k=i_1 \\ k\neq j}}^{i_N} \left[p_{\pi,i} \cdot \beta^2_{\sigma,ik}(r_{ik}) \cdot \sin^2\theta_{jik} + \left(1 + \cos^2\theta_{jik}\right) \cdot \beta^2_{\pi,ik}(r_{ik})\right] \tag{16}$$

$$\begin{aligned} \beta^4_{\pi,ij}(r_{ij})\cdot\Phi_{4\pi,ij} = {} & \frac{1}{4}\sum_{\substack{k=i_1 \\ k\neq j}}^{i_N} \sin^4\theta_{jik}\cdot\widehat{\beta}^{\,4}_{ik}(r_{ik}) + \frac{1}{4}\sum_{\substack{k=j_1 \\ k\neq i}}^{j_N} \sin^4\theta_{ijk}\cdot\widehat{\beta}^{\,4}_{jk}(r_{jk}) \\ & + \frac{1}{2}\sum_{\substack{k=i_1 \\ k\neq j}}^{i_N}\sum_{\substack{k'=k+1 \\ k'\neq j}}^{i_N} \sin^2\theta_{jik}\cdot\sin^2\theta_{jik'}\cdot\widehat{\beta}^{\,2}_{ik}(r_{ik})\cdot\widehat{\beta}^{\,2}_{ik'}(r_{ik'})\cdot\cos(\Delta\psi_{kk'}) \\ & + \frac{1}{2}\sum_{\substack{k=j_1 \\ k\neq i}}^{j_N}\sum_{\substack{k'=k+1 \\ k'\neq i}}^{j_N} \sin^2\theta_{ijk}\cdot\sin^2\theta_{ijk'}\cdot\widehat{\beta}^{\,2}_{jk}(r_{jk})\cdot\widehat{\beta}^{\,2}_{jk'}(r_{jk'})\cdot\cos(\Delta\psi_{kk'}) \\ & + \frac{1}{2}\sum_{\substack{k'=i_1 \\ k'\neq j}}^{i_N}\sum_{\substack{k=j_1 \\ k\neq i}}^{j_N} \sin^2\theta_{jik'}\cdot\sin^2\theta_{ijk}\cdot\widehat{\beta}^{\,2}_{ik'}(r_{ik'})\cdot\widehat{\beta}^{\,2}_{jk}(r_{jk})\cdot\cos(\Delta\psi_{kk'}) \end{aligned} \tag{17}$$

With

$$\widehat{\beta}_{ik}^{2}(r_{ik}) = p_{\pi,i} \cdot \beta_{\sigma,ik}^{2}(r_{ik}) - \beta_{\pi,ik}^{2}(r_{ik}) \quad (18)$$

The $\beta_{\pi,\mathrm{ij}}^{4}(r_{\mathrm{ij}}) \cdot \Phi_{4\pi,\mathrm{ij}}$ term contains four-body dihedral angles $\Delta\psi_{kk'}$ important in π bonding, and can be calculated as

$$\cos(\Delta\psi_{kk'}) = \begin{cases} \dfrac{2\left(\cos\theta_{kik'} - \cos\theta_{jik'} \cdot \cos\theta_{jik}\right)^2}{\sin^2\theta_{jik} \cdot \sin^2\theta_{jik'}} - 1 \quad or \\ \dfrac{2\left(\dfrac{\overrightarrow{ik'} \cdot \overrightarrow{jk}}{\left|\overrightarrow{ik'}\right| \cdot \left|\overrightarrow{jk}\right|} + \cos\theta_{ijk} \cdot \cos\theta_{jik'}\right)^2}{\sin^2\theta_{ijk} \cdot \sin^2\theta_{jik'}} - 1 \end{cases} \quad (19)$$

For more detailed discussion and descriptions of all equations, please see [7].

The BOP parameterization of CdTe can be done independently for elemental Cd, elemental Te, and finally for CdTe. As stated above, the ability to capture crystalline growth is a critical component of a high-fidelity interatomic potential. In general, a more transferrable (flexible for many phases) potential is more difficult to parameterize for capturing crystalline growth because the properties of various phases vary more dramatically with changes of the parameters.

Since the refined parameterization only updates the portions of the potential containing CdTe interactions many of the parameters remain consistent with the previous potentials [7, 8]. This particular fitting process includes a total of 40 parameters. However, many parameters can be fixed prior to the fitting process. ζ_1-ζ_4, r_0, r_c, r_1, r_{cut}, c_σ, a_π, f_σ, k_σ, g_0 are all chosen before optimizing the remaining parameters (see [7] for details). This leaves 25 parameters to be determined.

References

1. Schlesinger TE, Toney JE, Yoon H, Lee EY, Brunett BA, Franks L, James RB (2001) Mater Sci Eng 32:103
2. Kazmerski LL (2006) J Electron Spectrosc Relat Phenom 150:105
3. Chou HC, Rohatgi A (1994) J Electron Mater 23:31
4. Potter MDG, Cousins M, Durose K, Halliday DP (2000) J Mater Sci Mater Electron 11:525
5. Szeles C (2004) Phys Status Solidi A 241:783
6. Bolotnikov AE, Camarda GS, Carini GA, Cui Y, Li L, James RB (2007) Nucl Instrum Methods Phys Res A 579:125
7. Ward DK, Zhou XW, Wong BM, Doty FP, Zimmerman JA (2012) Phys Rev B 85:115206
8. Ward DK, Zhou XW, Wong BM, Doty FP, Zimmerman JA (2012) Phys Rev B 86:245203
9. Zhou XW, Ward DK, Wong BM, Doty Phys FP (2012) Rev Lett 108: 245503
10. Chaves JJ, Ward DK, Wong BM, Doty FP, Cruz-Campa JL, Nielson GN, Gupta VP, Zubia D, McClure J, Zhou XW (2012) Phys Rev B 85:245316
11. Zhou XW, Ward DK, Wong BM, Doty FP, Zimmerman JA, Nielson GN, Cruz-Campa JL, Gupta VP, Granata JE, Chavez JJ, Zubia D (2012) Phys Rev B 85:245302
12. Zhou XW, Ward DK, Wong BM, Doty FP, Zimmerman JA (2012) J Phys Chem C 116:17563
13. Plimpton S (1995) J Comput Phys 117:1
14. Pettifor DG, Oleinik II (1999) Phys Rev B 59:8487
15. Murdick DA, Zhou XW, Wadley HNG, Nguyen-Manh D, Drautz R, Pettifor DG (1999) Phys Rev B 59:8487
16. Drautz R, Nguyen-Manh D, Murdick DA, Zhou XW, Wadley HNG, Pettifor DG (2004) TMS Lett 1:31
17. Oh J, Grein CH (1998) J Cryst Growth 193:241
18. Borges DS, Rino JP (2005) Phys Rev B 72:014107
19. Kanoun MB, Merad AE, Aourag H, Cibert J, Merad G (2003) Solid State Sci 5:1211
20. Wang J, Rockett A (1991) Phys Rev B 43:12571
21. Ward DK, Zhour XW, Wong BM, Doty FP, Zimmerman JA (2011) J Chem Phys 134:244703
22. Barin I (1993) Thermochemical data of pures substances. Weinheim, VCH
23. Goodwin L, Skinner AJ, Pettifor DG (1989) Europhys Lett 9:701
24. Albe K, Nordlund K, Nord J, Kuronen A (2002) Phys Rev B 66: 035205
25. Wolfram S (2004) The mathematica book, 5th edn. Wolfram Research, Champaign
26. Hestenes MR, Stiefel E (1952) J Res Natl Bur Stand 49:409
27. Olsson DM, Nelson LS (1975) Technometrics 17:45
28. Storn R, Price K (1997) J Glob Opt 11:341
29. Kirkpatrick S, Gelatt CD, Vecchi MP (1983) Science 220:671
30. Perdew JP, Burke K, Ernzerhof M (1996) Phys Rev Lett 77:3865
31. Grimme S (2006) J Comput Chem 27:1787
32. Wong BM, Ye SH (2011) Phys Rev B 84:075115
33. Donnay JDH, Ondik HM (1973) Crystal data, determinative tables, vol 2, 3rd edn. US Department of Commerce, National Bureau of Standards, and Joint Committee on Power Diffraction Standards, Washington DC
34. Agrawal BK, Agrawal S (1992) Phys Rev B 45:8321
35. Rowe JM, Nicklow RM, Price DL, Zanio K (1974) Phys Rev B 10: 671
36. Grigoriev IS, Meilikhov EZ (1997) Handbook of physical quantities. CRC, New York